ELSEVIER

Resolution of complex tissue microarchitecture using the diffusion orientation transform (DOT)

Evren Özarslan,[a],* Timothy M. Shepherd,[b] Baba C. Vemuri,[a]
Stephen J. Blackband,[b,c] and Thomas H. Mareci[d]

[a]Department of Computer and Information Science and Engineering, University of Florida, P.O. Box 116120, Gainesville, FL 32611, USA
[b]Department of Neuroscience, University of Florida, P.O. Box 100244, Gainesville, FL 32610, USA
[c]National High Magnetic Field Laboratory, Tallahassee, FL 32310, USA
[d]Department of Biochemistry and Molecular Biology, University of Florida, P.O. Box 100245, Gainesville, FL 32610, USA

This article describes an accurate and fast method for fiber orientation mapping using multidirectional diffusion-weighted magnetic resonance (MR) data. This novel approach utilizes the Fourier transform relationship between the water displacement probabilities and diffusion-attenuated MR signal expressed in spherical coordinates. The radial part of the Fourier integral is evaluated analytically under the assumption that MR signal attenuates exponentially. The values of the resulting functions are evaluated at a fixed distance away from the origin. The spherical harmonic transform of these functions yields the Laplace series coefficients of the probabilities on a sphere of fixed radius. Alternatively, probability values can be computed nonparametrically using Legendre polynomials. Orientation maps calculated from excised rat nervous tissue data demonstrate this technique's ability to accurately resolve crossing fibers in anatomical regions such as the optic chiasm. This proposed methodology has a trivial extension to multiexponential diffusion-weighted signal decay. The developed methods will improve the reliability of tractography schemes and may make it possible to correctly identify the neural connections between functionally connected regions of the nervous system.
© 2006 Elsevier Inc. All rights reserved.

Introduction

The diffusional attenuation of MR signal in pulsed field gradient experiments (Stejskal and Tanner, 1965) has been exploited to

characterize diffusional anisotropy in fibrous tissues like muscle (e.g. Cleveland et al., 1976) and white matter in animal (e.g. Moseley et al., 1990) and human (e.g. Chenevert et al., 1990) nervous tissue. When the narrow pulse condition is met, i.e. the duration of the applied diffusion sensitizing gradients (δ) is much smaller than the time between the two pulses (Δ), the fundamental relationship between the MR signal attenuation and average displacement probabilities $P(\boldsymbol{R})$ is given by a Fourier integral (Callaghan, 1991):

$$P(\boldsymbol{R}) = \int E(\boldsymbol{q}) \, \exp(-2\pi i \boldsymbol{q} \cdot \boldsymbol{R}) d\boldsymbol{q}, \qquad (1)$$

where $\boldsymbol{R}$ is the displacement vector and $\boldsymbol{q}$ is the reciprocal space vector defined by $\boldsymbol{q} = \gamma \delta \boldsymbol{G}/2\pi$, where γ is the gyromagnetic ratio and $\boldsymbol{G}$ is the gradient vector. In the above expression $E(\boldsymbol{q}) = S(\boldsymbol{q})/S_0$, where $S(\boldsymbol{q})$ is the signal value associated with the reciprocal space vector $\boldsymbol{q}$ and S_0 is the signal when no diffusion gradient is applied, i.e. when $\boldsymbol{q} = 0$.

Diffusional anisotropy is well-reflected in the water displacement probabilities, and it is expected that, in fibrous tissues, the orientations specified by large displacement probabilities will coincide with the fiber orientations. One could in principle estimate these displacement probability functions by using Eq. (1) and the fast Fourier transform (FFT), however, this would require data points all across the space spanned by the diffusion gradients (or $\boldsymbol{q}$ vectors). This q-space approach would require very high gradient strengths and long acquisition times that are difficult to achieve in clinical settings (Basser, 2002). Although attempts have been made to acquire such data sets in vivo (Wedeen et al., 2000), the results typically suffer from undersampled q-space and sacrificed spatial resolution.

More than a decade ago, Basser et al. (1994a,b) introduced an imaging method called diffusion tensor imaging (DTI) that replaced the apparent diffusion coefficients that had been calculated in diffusion-weighted imaging studies with a symmetric, positive-

definite, second-order tensor. This model required only 7 diffusion-weighted images with clinically feasible diffusion gradient strengths. This approach enabled simple estimation of diffusional anisotropy and predicted a fiber orientation specified by the principal eigenvector of the diffusion tensor. Despite its modest requirements, the results achieved using DTI have been very successful in regions of the brain and spinal cord with substantial white matter coherence and have enabled the mapping of some anatomical connections in the central nervous system (e.g. Conturo et al., 1999; Mori et al., 1999; Basser et al., 2000).

DTI assumes a displacement probability characterized by an oriented Gaussian probability distribution function (PDF) whose covariance matrix is proportional to the diffusion tensor. Such a PDF has only one orientational mode and, as such, cannot resolve more than one fiber orientation inside a voxel. This shortcoming of DTI has prompted interest in the development of more sophisticated models. Tuch et al. (1999) introduced a high angular resolution diffusion imaging (HARDI) method that suggested that the apparent diffusion coefficients could be evaluated along many orientations independently without fitting a "global" function to the data, i.e. using the Stejskal–Tanner expression (Stejskal, 1965):

$$E(\boldsymbol{u}) = e^{-bD(\boldsymbol{u})}, \tag{2}$$

where $\boldsymbol{u}$ is a unit vector specifying the direction of the diffusion sensitizing gradient and $E(\boldsymbol{u})$ is the signal attenuation value on a sphere in q-space whose radius is related to the diffusion weighting factor b (where $b = 4\pi q^2 t$ and $t = \Delta - \delta/3$ is the effective diffusion time). The result is an angular distribution of apparent diffusivities, $D(\boldsymbol{u})$, herein referred to as the diffusivity profile. It has been shown that the diffusivity profile has a complicated structure in voxels with orientational heterogeneity (von dem Hagen and Henkelman, 2002; Tuch et al., 2002). Several studies proposed to represent the diffusivity profile using a spherical harmonic expansion (Frank, 2002; Alexander et al., 2002). A schematic description of this approach is given below:

$$D(\boldsymbol{u}) \underset{\text{LS}}{\overset{\text{SHT}}{\rightleftarrows}} a_{lm}, \tag{3}$$

where SHT and LS stand for spherical harmonic transform and Laplace series respectively.

However, one major difficulty with employing HARDI in studies involving orientation mapping has been that the peaks of the diffusivity profile do not necessarily yield the orientations of the distinct fiber populations (Fig. 1). Özarslan and Mareci (2003) have shown that the (SHT) approach could be seen as a generalization of DTI since the coefficients of the Laplace series (obtained from the SHT of the diffusivity profile) are related to the components of higher-order Cartesian tensors. Later, Özarslan et al. (2004a,b) proposed to use the higher-order Cartesian tensors to generate signal values (assuming exponential attenuation) on the three-dimensional q-space and evaluated an FFT to approximate the displacement probabilities. Jansons and Alexander (2003) proposed a method to calculate a displacement probability map from HARDI data sets by enforcing the unusual condition that the probabilities are nonzero only on a spherical shell. Although the results are encouraging, both of these schemes are computationally expensive.

Another generalization of DTI that employs higher-order Cartesian tensors was proposed by Liu et al. (2003). This approach necessitates sampling of q-space in several spherical shells, undesirably increasing the required number of acquisitions.
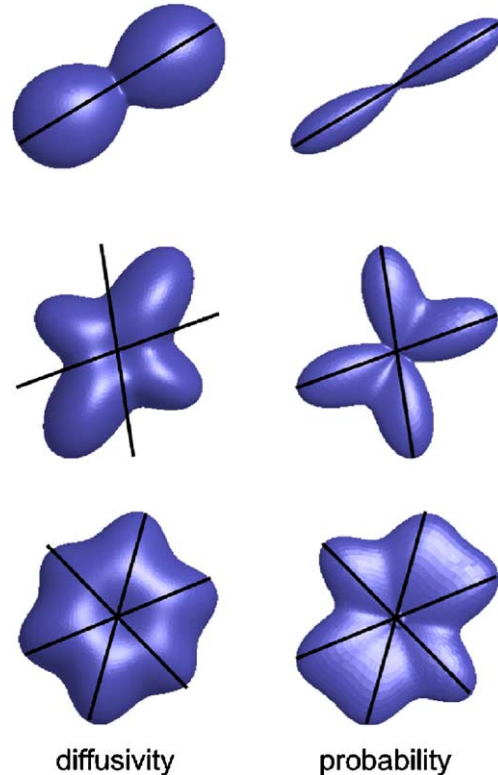

Fig. 1. Apparent diffusivity (left column) and displacement probability (right column) profiles calculated from simulations of 1-, 2- and 3-fiber systems (top to bottom). Black lines depict the exact orientations of the simulated fibers specified by the azimuthal angles $\phi_1 = 30$, $\phi_2 = \{20°, 100°\}$ and $\phi_3 = \{20°, 75°, 135°\}$ for the 1-, 2- and 3-fiber systems respectively. Polar angles for all fibers were taken to be 90° so that all fibers lie on the image plane. The peaks of the diffusivity profile do not necessarily yield the orientations of the distinct fiber populations. This can sometimes lead to erroneous fiber structure interpretation from HARDI data.

Furthermore, it is difficult to reliably extract the phase of the MR signal required by this scheme. Tuch et al. (2003) proposed a method in which the radial integral of the displacement PDF is obtained by the spherical Radon transform. This scheme provides an approximation to the true radial integral because the result is a convolution of the probability values with a 0-th order Bessel function (Tuch, 2004) that may give rise to an undesirable "contamination" of the probability along one direction with probabilities from other directions. Finally, there have been several studies that have modeled diffusion using multicompartmental models. These studies assume distinct fiber populations with no exchange. Moreover, the number of such compartments has to be prespecified (Inglis et al., 2001; Parker and Alexander, 2003; Maier et al., 2004; Assaf et al., 2004) or the signal from each fiber population is undesirably forced to have prespecified attributes (such as anisotropy) (Tournier et al., 2004).

In this work, we introduce a new method, called the diffusion orientation transform (DOT), that describes how the diffusivity profiles can be transformed into probability profiles. Our method is based on the HARDI acquisition scheme and can be extended to more general acquisition strategies. We express Eq. (1) in spherical coordinates then, under the monoexponential attenuation assumption, evaluate the radial part of the integral analytically. The probability values on a fixed radius can be reconstructed either

directly or parametrically in terms of a Laplace series. We prove that this expansion converges to the true probability profile. Our technique can be regarded as a transformation of diffusivity to probability profiles whose peaks correspond to distinct fiber orientations (Fig. 1). Our method is robust and fast. Although we present results on excised, chemically fixed rat nervous tissue, the requirements of our method make it suitable for the clinical environment. We discuss our assumption that the MR signal decays monoexponentially and further demonstrate that a trivial extension to multiexponential attenuation results in improved reconstruction of the probabilities.

Theory

In this section, we show that, starting from the signal attenuations of a HARDI acquisition, it is possible to calculate the orientation maps without the need to fit a particular model to the data. We achieve this by two different approaches.

Parametric reconstruction

The Fourier transform that relates the signal attenuation to the water displacement probability Eq. (1) can be written in spherical coordinates. This is a consequence of the pointwise convergent expansion of the plane wave in spherical coordinates (Schwabl, 1989) given by

$$e^{\pm 2\pi i \boldsymbol{q} \cdot \boldsymbol{R}} = 4\pi \sum_{l=0}^{\infty} \sum_{m=-1}^{l} (\pm i)^l j_l(2\pi qr) Y_{lm}(\boldsymbol{u})^* Y_{lm}(\boldsymbol{r}), \quad (4)$$

where $\boldsymbol{q} = q\boldsymbol{u}$ and $\boldsymbol{R} = r\boldsymbol{r}$, with $q = |\boldsymbol{q}|$ and $r = |\boldsymbol{R}|$. Note that $j_l(2\pi qR)$ is the l-th order spherical Bessel function whereas $Y_{lm}(\boldsymbol{u})$ is the spherical harmonic function. Inserting this expression into Eq. (1), we get

$$P(R_0\boldsymbol{r}) = \sum_{l=0}^{\infty} \sum_{m=-l}^{l} (-i)^l Y_{lm}(\boldsymbol{r}) \int d\boldsymbol{u} Y_{lm}(\boldsymbol{u})^* I_l(\boldsymbol{u}), \quad (5)$$

where

$$I_l(\boldsymbol{u}) = 4\pi \int_0^{\infty} dq q^2 j_l(2\pi qR_0) \exp\left(-4\pi^2 q^2 t D(\boldsymbol{u})\right). \quad (6)$$

Here, r was set to a particular radius R_0, and it is assumed that signal attenuates along each radial line in q-space as described by the Stejskal–Tanner relationship given in Eq. (2). Note that the function $P(R_0\boldsymbol{r})$ is not the isosurface of the three-dimensional displacement probability function, but it is the probability of finding the particle, initially at the origin, at the point $R_0\boldsymbol{r}$, that is, we will be interested in the probability values on a sphere of radius R_0.

The integral in Eq. (6) can be evaluated analytically which makes it possible to efficiently compute the values of the $I_l(\boldsymbol{u})$ function. See Appendix A for a detailed description. Since $I_l(\boldsymbol{u})$ is a function of orientation, we can expand it in a Laplace series, i.e.

$$I_l(\boldsymbol{u}) = \sum_{l'=0}^{\infty} \sum_{m'=-l'}^{l'} \alpha_{l'm'} Y_{l'm'}(\boldsymbol{u}), \quad (7)$$

where the coefficients $\alpha_{llm'}$ are given by an SHT,

$$\alpha_{l'm'} = \int Y_{l'm'}(\boldsymbol{u})^* I_l(\boldsymbol{u}) d\boldsymbol{u}. \quad (8)$$

Comparing the integration over $\boldsymbol{u}$ in Eq. (5) with the expression in Eq. (8), it can be seen that $P(R_0\boldsymbol{r})$ has the Laplace series expansion

$$P(R_0\boldsymbol{r}) = \sum_{l=0}^{\infty} \sum_{m=-l}^{l} p_{lm} Y_{lm}(\boldsymbol{r}) \quad (9)$$

with

$$p_{lm} = (-i)^l \alpha_{llm} = (-1)^{1/2} \alpha_{llm}, \quad (10)$$

where in the last step we have used the fact that l is even. The convergence of the resulting series in Eq. (5) to the desired probability value is proved in Appendix D. Note that the coefficients of this Laplace series for a particular value of l come from the l-th order Laplace series coefficients of $I_l(\boldsymbol{u})$.

Implementation aspects

In summary, given the HARDI data, the estimation of the probability of finding the particle at the point $R_0\boldsymbol{r}$ away from the origin involves the following steps:

(1) Compute the diffusivity $D(\boldsymbol{u})$ along each direction using Eq. (2).
(2) Then, compute $I_l(\boldsymbol{u})$ using Eq. (27) or Eq. (28) with Table 2.
(3) For each l, compute α_{llm}, the l-th order spherical harmonic transform of $I_l(\boldsymbol{u})$.
(4) Then, evaluate Eq. (9).

Implementation of the items 1, 2 and 4 above are trivial. Our data acquisition scheme involves sampling the sphere on the vertices of a tessellated icosahedron. With this method, 46 or 81 points are sampled on the unit hemisphere from second- or third-order tessellations respectively. Following Ritchie and Kemp (1999), we compute the spherical harmonic transform given in Eq. (8) by discretizing the integrals on the sphere with integration weights calculated from the areas of the polygons specified by the dual tessellation. We also exploit the fact that the probabilities are real. This condition ensures that the expression

$$p_{l(-m)} = (-1)^m p_{lm}^* \quad (11)$$

holds. Thus, it is unnecessary to evaluate the integrals that generate p_{lm} coefficients with negative m values. The calculation of the α_{llm} coefficients takes only 25 to 60 s for the entire data set, depending on the matrix size and number of angular samples, when using a modest Athlon XP 1800 processor (AMD, Sunnyvale, CA).

Schematic description of the method is described below. Note that this is our revision of Eq. (3) provided in the Introduction section.

$$D(\boldsymbol{u}) \xrightarrow{\text{Eq.(28)}} I_l(\boldsymbol{u}) \xrightarrow{\text{SHT}} \alpha_{llm} \xrightarrow{\times (-1)^{l/2}} p_{lm} \xrightarrow{\text{LS}} P(R_0\boldsymbol{r}) \quad (12)$$

Nonparametric reconstruction

An alternative form to the Rayleigh expansion in Eq. (4) is given by

$$e^{\pm 2\pi i \boldsymbol{q} \cdot \boldsymbol{R}} = \sum_{l=0}^{\infty} (\pm i)^l (2l+1) j_l(2\pi qr) P_l(\boldsymbol{u} \cdot \boldsymbol{r}), \quad (13)$$

which is just a consequence of the addition theorem for spherical harmonics provided in Eq. (42). In Eq. (13), P_l is the l-th order Legendre polynomial. Employing this form of the Rayleigh expansion in our formalism does not change the radial integral,

and the probability values are given by

$$
\begin{aligned}
P(R_0\boldsymbol{r}) &= \tfrac{1}{4\pi} \sum_{l=0}^{\infty} (-i)^l (2l+1) \int d\boldsymbol{u} I_l(\boldsymbol{u}) P_l(\boldsymbol{u} \cdot \boldsymbol{r}) \\
&= \sum_{l=0}^{\infty} \int d\boldsymbol{u}(-1)^{1/2} \frac{2l+1}{4\pi} P_l(\boldsymbol{u} \cdot \boldsymbol{r}) I_l(\boldsymbol{u}),
\end{aligned}
\tag{14}
$$

with the definition of I_l as in Eqs. 6, 27, 28.

The above expression provides an alternate estimation of the results that could be obtained from the parametric reconstruction. The schematic description of the nonparametric reconstruction is given by

$$
D(\boldsymbol{u}) \xrightarrow{\text{Eq.(28)}} I_l(\boldsymbol{u}) \xrightarrow{\text{Eq.(14)}} P(R_0\boldsymbol{r})
\tag{15}
$$

The above formulation can be easily expressed in matrix form. Suppose that the HARDI experiment is performed with diffusion sensitizing gradients applied along N_G directions. The direction describing the j-th gradient will be represented with the unit vector $\boldsymbol{u}_j$. Similarly, let $\boldsymbol{r}_i$ denote the unit vector describing the i-th direction along which the probability will be estimated where the total number of such directions is N_R. Then, Eq. (14) can be expressed simply by

$$
\boldsymbol{T} = \sum_{l=0}^{\infty} \mathbf{M}_l \boldsymbol{Z}_l,
\tag{16}
$$

where $\boldsymbol{T}$ is the N_R dimensional vector of probabilities. In Eq. (16), the components of the N_G dimensional vector $\boldsymbol{Z}_l$ are given by

$$
(\boldsymbol{Z}_l)_j = I_l(\boldsymbol{u}_j),
\tag{17}
$$

and the components of the $N_R \times N_G$ dimensional matrix $\mathbf{M}_l$ are given by

$$
(\mathbf{M}_l)_{ij} = \frac{w_j}{4\pi}(-1)^{l/2}(2l+1)P_l(\boldsymbol{u}_j \cdot \boldsymbol{r}_i),
\tag{18}
$$

where w_j are the integration weights associated with each of the gradient directions. Note that the matrices $\mathbf{M}_l$ can be computed once for each gradient sampling scheme. Therefore, the only computational burden comes from the pixel-by-pixel estimation of $I_l(\boldsymbol{u}_j)$ (which is a straight forward operation) and the matrix multiplication in Eq. (16).

Parametric vs. nonparametric reconstruction

We have provided two methods for the reconstruction of probability profiles. The first approach yielded the components of a spherical tensor, where each component, p_{lm}, is a characteristic of the distribution $P(R_0\boldsymbol{r})$ since it is equal to the spherical correlation of the distribution with the complex conjugate of the corresponding spherical harmonic $Y_{lm}(\boldsymbol{r})$. Therefore, this approach was named the "parametric" reconstruction. The parametric reconstruction enables one to express the probabilities in terms of a Laplace series, whereas the nonparametric reconstruction provided the probability values directly. It is simpler to implement the latter scheme as no SHT transform is necessary. However, when the Laplace series is terminated at $l = l_{\max}$, the parametric reconstruction expresses the probability values in terms of $(l_{\max} + 1)(l_{\max} + 2)/2$ numbers, which are typically much smaller than the number of directions along which the probabilities are estimated (N_R) when one visualizes the probability surfaces. This enables more feasible storage of the probability profiles in computer memory.

Using either one of the schemes, once the probability values are evaluated along many points, the following parametrized surface can be visualized (see Fig. 1):

$$
\boldsymbol{X}(\theta, \phi) = P(R_0\boldsymbol{r})\boldsymbol{r} = P(\theta, \phi)
\begin{pmatrix}
\sin\theta \, \cos\phi \\
\sin\theta \, \sin\phi \\
\cos\theta
\end{pmatrix},
\tag{19}
$$

where θ is the polar and ϕ is the azimuthal angle associated with the unit vector $\boldsymbol{r}$.

Scalar indices

Many clinical studies employ scalar rotationally invariant measures derived from diffusion MRI data to quantify the changes occurring with development and pathologies. Recently, Özarslan et al. (2005) demonstrated that generalized models more accurately quantify anisotropy measures compared to DTI. In this section, we discuss the estimation of the generalized scalar indices from the probability values evaluated using DOT and demonstrate the images constructed by computing these measures on a pixel-by-pixel basis. For completeness, formulation of anisotropy in terms of both variance and entropy is provided.

Anisotropy from variance

In Özarslan et al. (2005), generalized anisotropy indices based on the variance of the values of an arbitrary integrable positive-definite function defined on the unit sphere were presented. When applied to functions represented in terms of spherical harmonics, like the parametrically reconstructed $P(R_0\boldsymbol{r})$ in this work, the variance takes a particularly simple form given by

$$
V = \frac{1}{9p_{00}^2} \sum_{l=2}^{\infty} \sum_{m=-l}^{l} |p_{lm}|^2.
\tag{20}
$$

Then, using the scaling relationship provided in Özarslan et al. (2005), it is possible to map the values of the variance to the interval (0, 1) where the resulting index is called generalized anisotropy (GA). Note that the GA index is based on variance and hence can be seen as a generalization of the relative anisotropy (RA) and fractional anisotropy (FA) indices commonly used in DTI analysis (Basser, 1995).

Anisotropy from entropy

The function defined on the sphere can be taken as a PDF simply by normalizing the integral of the probability profile over the sphere via a multiplication of the p_{lm} coefficients by $1/\sqrt{4\pi}p_{00}$. Then, it is meaningful to define the entropy associated with this distribution. By using the expression in Özarslan et al. (2005) for the entropy of a general function on the unit sphere, it is possible to show that the entropy in our case is given by[1]

$$
\begin{aligned}
\sigma &= \ln(4\pi\langle P(R_0\boldsymbol{r})\rangle) - \frac{1}{4\pi\langle P(R_0\boldsymbol{r})\rangle} \int d\boldsymbol{r} P(R_0\boldsymbol{r}) \ln P(R_0\boldsymbol{r}) \\
&= \ln\left(\sqrt{4\pi}p_{00}\right) - \frac{1}{\sqrt{4\pi}p_{00}} \sum_{l=0}^{\infty} \sum_{m=-l}^{l} p_{lm}^* \lambda_{lm},
\end{aligned}
\tag{21}
$$

---

[1] The expression for the entropy is a slightly modified version of the expression in Özarslan et al. (2005), where the 3 in the argument of the natural logarithm is replaced by 4π. The reason for this modification stems from the difference between the normalization conditions imposed on the functions $D_N(\boldsymbol{u})$ in Özarslan et al. (2005) and $P(R_0\boldsymbol{r})$ in this work.
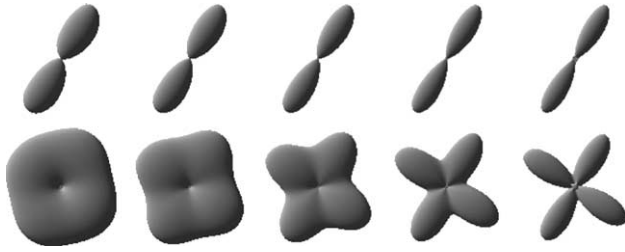
Fig. 2. Probability maps estimated on a sphere of radius 8 to 16 μm in equal steps of 2 μm (from left to right). Top row shows these surfaces when there is only one orientation, where the bottom row shows them from a voxel with two distinct orientations. As the radius of the sphere on which the probability values are estimated is increased, the two fiber orientations are better resolved.

where λ_{lm} are given by the SHT of $\ln P(R_0 \mathbf{r})$. Similar to the transformation of variance values into the GA index, the entropy values can be transformed into an anisotropy index that was called scaled entropy (SE) (Özarslan et al., 2005).

Simulations

We have applied the scheme described above to the simulations of single fiber and crossing fiber systems. The diffusion-weighted MR signal attenuation from molecules, with free diffusion coefficient given by D_0, restricted inside a cylinder of radius ρ and length L, when the applied diffusion gradient makes an angle ϑ with the orientation of the cylinder, is given by Söderman and Jönsson (1995):

$$
E(\mathbf{q}) = \sum_{n=0}^{\infty} \sum_{k=1}^{\infty} \sum_{m=0}^{\infty} \frac{2K_{nm}\rho^2(2\pi q\rho)^4 \sin^2(2\vartheta)\gamma_{km}^2}{\left[(n\pi\rho/L)^2 - (2\pi q\rho\,\cos\vartheta)^2\right]^2}
$$

$$
\times \frac{[1 - (-1)^n\cos(2\pi qL\cos\vartheta)][J_m'(2\pi q\rho\,\sin\vartheta)]^2}{L^2\left[\gamma_{km}^2 - (2\pi q\rho\,\sin\vartheta)^2\right]^2(\gamma_{km}^2 - m^2)}
$$

$$
\times \exp\left(-\left[\left(\frac{\gamma_{km}}{\rho}\right)^2 + \left(\frac{n\pi}{L}\right)^2\right]D_0\Delta\right). \tag{22}
$$

In this expression, J_m is the m-th order Bessel function, γ_{km} is the k-th solution of the equation $J_n'(\gamma) = 0$ with the convention

$\gamma_{10} = 0$, and $K_{nm} = \delta_{n0}\delta_{m0} + 2[(1 - \delta_{n0}) + (1 - \delta_{m0})]$. In the presence of more than one cylinder, the signal attenuations from these cylinders become additive. This way, multiple fiber orientations can be modeled assuming that diffusing molecules are constrained within these cylinders with no possibility for exchange between different cylinders. This system provides a simplified view of the neural tissue in the slow exchange assumption which is likely to be the case in short diffusion times. Although diffusional processes within real neural tissue will be much more complicated than what can be achieved through simulations, currently, they still provide a suitable test bed for the schemes developed to address the problem.

We have evaluated Eq. (22), with the parameters: $L = 5$ mm, $\rho = 5$ μm, $D_0 = 2.02 \times 10^{-3}$ mm^2/s, $\Delta = 20.8$ ms, $\delta = 2.4$ ms, $b = 1500$ s/mm^2. These parameters resemble our typical imaging protocol on excised rat brains. Similar to that in von dem Hagen and Henkelman (2002), we terminated the infinite series in Eq. (22) at $n = 1000$ and k, $m = 10$. Similar to a HARDI experiment protocol, the gradient directions were chosen to point toward the 81 vertices of the third-order tessellations of an icosahedron on a unit hemisphere.

As already shown in Fig. 1, we have computed the probability profiles from fiber configurations whose orientations are specified by the azimuthal angles $\phi_1 = 30°$, $\phi_2 = \{20°, 100°\}$ and $\phi_3 = \{20°, 75°, 135°\}$ for the 1-, 2- and 3-fiber systems respectively. Polar angles for all fibers were taken to be 90° so that a view from the z axis will clearly depict the individual fiber orientations. Computations with other polar angles yielded similar quality results. In all computations, the Laplace series were terminated after $l = 8$.

Fig. 2 shows the effect of varying R_0 on the constructed probability surfaces. Increasing R_0 gives rise to the sharpening of the displacement PDFs. This could be predicted from Fig. 17a that indicates that for small R_0 the largest contribution comes from I_0, which upon the spherical harmonic transform forms the isotropic part of the constructed probabilities. When R_0 is greater than the radius of the cylinder confining the water molecules and the characteristic length $\sqrt{6Dt}$ associated with the diffusion process (which is 15 μm for the system in Fig. 17a), the distribution of probability on the surface becomes sharper and individual fiber populations are better resolved.
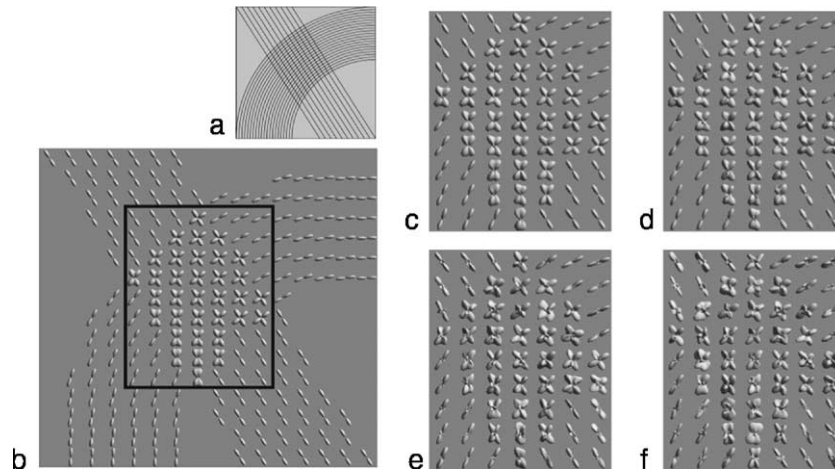

Fig. 3. (a) Simulated system of two crossing fiber bundles. (b) Probability surfaces computed using the expansion of the probability on the surface of a sphere. (c–f) Surfaces in the framed area of panel b recomputed under increasing levels of noise added to the signal values. These panels represent images with signal-to-noise ratios (SNRs) between 50:1 and 12.5:1 in the non-diffusion-weighted image.

Table 1
The angle between the computed and true fiber orientations (deviation angles) in degrees

	ψ ($\sigma = 0$)	ψ ($\sigma = 0.02$)	ψ ($\sigma = 0.04$)	ψ ($\sigma = 0.06$)	ψ ($\sigma = 0.08$)
1 fiber	{0.364}	0.77 ± 0.42	1.44 ± 0.79	2.20 ± 1.09	3.08 ± 1.66
2 fibers	{1.43, 0.80}	2.33 ± 1.10	3.66 ± 2.01	6.00 ± 5.57	8.07 ± 7.92
3 fibers	{2.87, 0.60, 4.57}	5.81 ± 5.84	11.5 ± 10.1	14.7 ± 10.3	17.6 ± 11.9

Second column presents the deviation angle of each fiber when the DOT of noiseless signal profile is taken. Columns 3–6 show the mean and standard deviation values for the deviation angle when Gaussian noise of standard deviation 0.02 to 0.08 (from left to right) was added to the signal profiles. The computations for the DOT of noisy signals were repeated 100 times.

We also computed the probability surfaces for a simulated image of fiber crossings shown in Fig. 3. The surfaces are consistent with the underlying known fibrous structure. The circular and linear fiber bundles were chosen so that a distribution of crossing angles is achieved across the region with orientational heterogeneity. The distinct fiber orientations are better resolved when the different fiber bundles make larger angles with each other. Fig. 3b shows the probability profiles when there is no noise added to the signal values. Similar to Jansons and Alexander (2003), we have added Gaussian noise of increasing standard deviation to the real and complex parts of the signal. When the signal intensity in the image with no diffusion weighting is taken to be centered around 1 and Gaussian noise of standard deviations 0.02 through 0.08 is added (in equal steps), the probability profiles shown in Figs. 3c–f are obtained. These panels represent images with signal-to-noise ratios (SNRs) between 50:1 and 12:5:1 in the non-diffusion-weighted (S_0) image. Note that, in our standard HARDI protocol, we obtain SNR values in excess of 30 in diffusion-weighted scans and about 100 in non-diffusion-weighted images. Therefore, in real experiments, one can expect to achieve results that will be of similar or better quality with the image presented in Fig. 3c.

To provide a more quantitative assessment of the DOT method and its sensitivity to increasing noise levels, we took the HARDI simulations of 1-, 2- and 3-fiber profiles presented in Fig. 1 and numerically computed the fiber orientations by finding the maxima of the probability profiles (see Table 1). In this table, ψ denotes the angle between the computed and the true fiber orientations in degrees whereas σ is the noise level. Note that, when no noise was introduced ($\sigma = 0$), there was a small deviation of the computed fiber direction from the true fiber orientation because of the finite sampling of the hemisphere (at 81 gradient orientations), the termination of the LS at order 8 and the precision of the numerical procedure used to compute the maxima of the probability profiles. The simulations of the signal profiles with noise were repeated 100 times for each noise level to provide a distribution of deviation angles. We report the mean and standard deviations of these distributions in columns 3–6 of Table 1. As expected, the ψ values increase with increasing noise, and it is more challenging to accurately resolve the distinct fiber orientations when there are more fiber orientations.

Imaging parameters

To test the performance of the DOT, we calculated the orientation probabilities on HARDI data from three anatomical regions of excised, perfusion-fixed rat nervous tissue (optic chiasm, brain and spinal cord). These experiments were performed with the approval of the University of Florida Institutional Animal Care and Use Committee. The images were acquired at 17.6 T (brain) or 14.1 T (spinal cord and optic chiasm) using Bruker Avance imaging systems. A diffusion-weighted spin echo pulse sequence was used. Diffusion-weighted images were acquired along 81 (brain) or 46 (spinal cord and optic chiasm) directions with a b-value of 1500 s/mm^2 (brain and spinal cord) or 1250 s/mm^2 (optic chiasm) along with a single image acquired at $b \approx 0$ s/mm^2. Echo times were 23, 28, 25 ms; repetition times were 0.5, 2, 1.17 s; Δ values were 12.4, 17.8 and 17.5 ms; δ values were 1.2, 2.2 and 1.5 ms; bandwidth was set to 35, 32 and 39 kHz; signal averages were 10, 6, 7; matrix sizes were 128 × 128 × 5, 100 × 100 × 60, 72 × 72 × 40 and resolutions were 33.6 × 33.6 × 200 μm^3, 150 × 150 × 300 μm^3, 60 × 60 × 300 μm^3 for optic chiasm, brain and spinal cord data respectively. The optic chiasm images were signal averaged to 67.2 × 67.2 × 200 μm^3 resolution prior to probability calculations. In Fig. 4, we show a particular axial slice from a HARDI data set collected from excised rat spinal cord.

Results

The probability maps were calculated by following the procedure described in the Theory section. Terms up to $l = 8$ were included in all calculations. Representative images of the $I_l(\boldsymbol{u})$ values, when $\boldsymbol{u}$ is chosen to point through the image plane, are presented in Fig. 5. Note that the intensity values in the $I_{10}(\boldsymbol{u})$ image are very small. The p_{lm} coefficients that generate the probability surfaces are shown in Fig. 6 for the same slice. It was not necessary to show the coefficients with negative m values because of Eq. (11). Note that this relationship also ensures that p_{l0} are real.

The computed p_{lm} components were used in the calculation of the scalar measures described in the previous section. In Fig. 7, we show the variance and GA maps computed from the optic chiasm and brain data sets. The GA index was calculated both from the p_{lm} coefficients and a second-order tensor fit to the data. It is apparent that, although the GA values are similar in the unidirectional section of the optic chiasm, in the region of decussating optic nerve fibers, GA values implied by DTI were lower than those calculated from the probability surfaces. Also included are the entropy (σ) and the SE maps calculated from both samples. It should be noted that V, GA, σ and SE values depend on the choice of R_0.

Visualization of the probability profiles was done by computing the probabilities along many directions and displaying the parametrized surface defined in Eq. (19). To increase the sharpness of the probability profiles, we have subtracted the minimum probability existing in the profile from all probability values. This
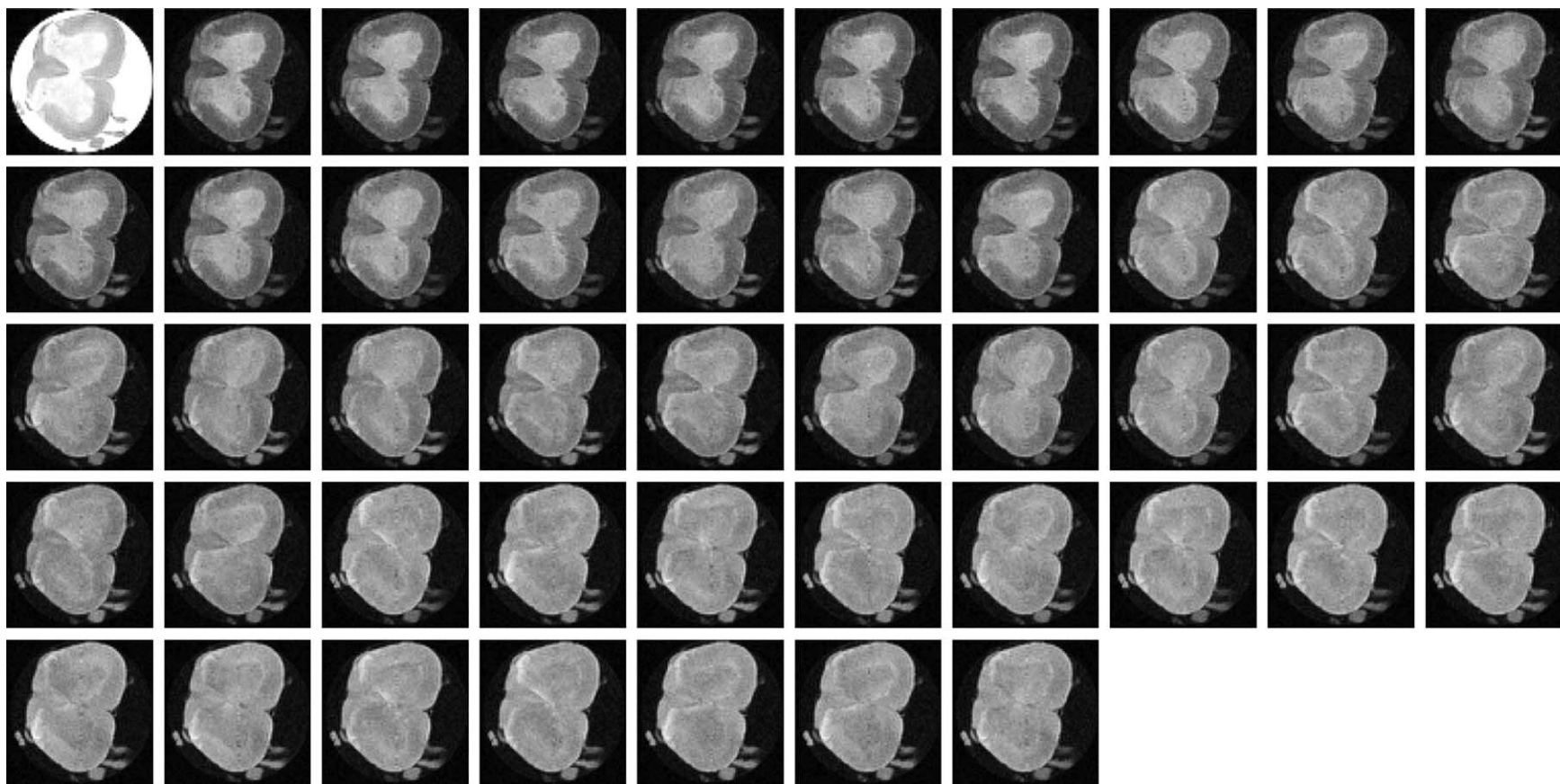
Fig. 4. Representative HARDI data set from an excised, perfusion-fixed rat spinal cord. At the upper left corner is the image with no diffusion weighting followed by 46 diffusion-weighted images.
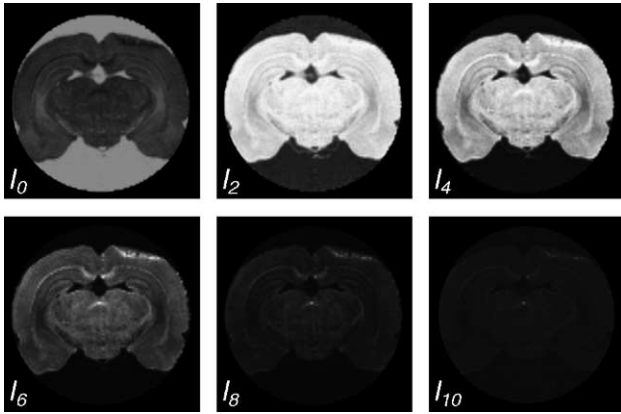
Fig. 5. $I_l(\boldsymbol{u})$ images up to $l = 10$ from coronal sections of rat brain when $\boldsymbol{u}$ is chosen to point through the image plane.

process was followed by a normalization of the surface to fill the cube (voxel) it will be located in so that all visualized surfaces have similar sizes. As a result, the visualized surfaces emphasize the directionality but are not intended to provide information on the true values for the probabilities.

We have overlaid these orientation surfaces on generalized anisotropy (GA) maps (Özarslan et al., 2005) computed from

the displacement probabilities as shown above. The coloring schemes proposed for DTI orientation visualization (Pajevic and Pierpaoli, 1999) are not readily applicable to probability surfaces. The "peakedness" on the image plane is obvious. However, one may miss the orientations through the image plane. To prevent this, we color-coded the surfaces such that, as the values of the z-component of the parametrized surface vary from the maximum probability value present in the probability profile to minus this maximum probability value, the color of the surface changes from green to blue. In all calculations, R_0 was set to 16 μm, and the last term kept in the Laplace series was $l = 8$.

The rat optic chiasm is a distinct white matter structure with both parallel and decussating optic nerve fibers, thus providing an excellent experimental validation for our approach. The top panel of Fig. 8 shows the diffusivity profile obtained from the diffusion-attenuated signal values. The bottom panel demonstrates the displacement probabilities computed from the diffusivity profiles using the DOT method. Every other pixel of the optic chiasm image was included for the sake of clarity. The diffusivity profiles fail to give meaningful results in the central region of the optic chiasm where fiber orientations are heterogeneous. The probability profiles, however, demonstrate the distinct fiber orientations in the central region of the optic chiasm where myelinated axons from the two optic nerves cross
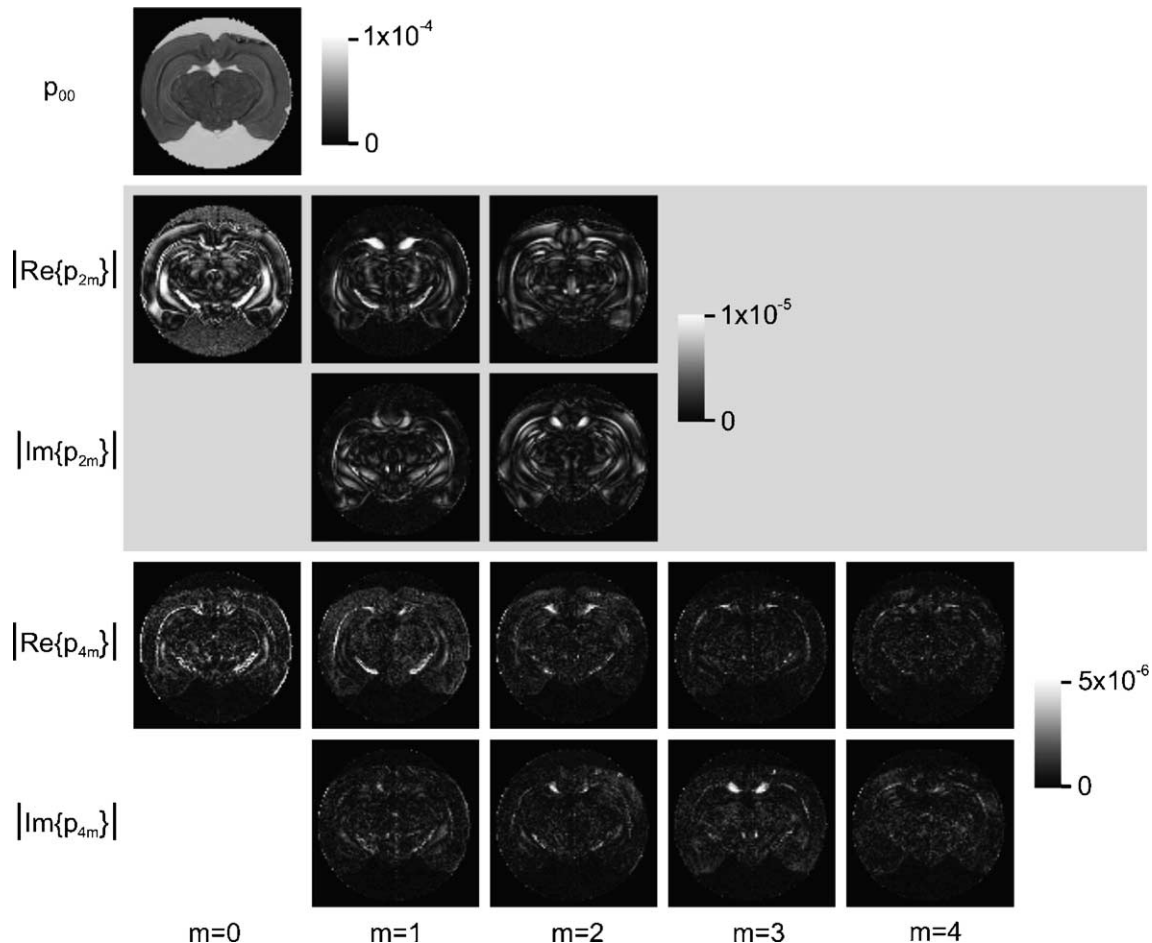

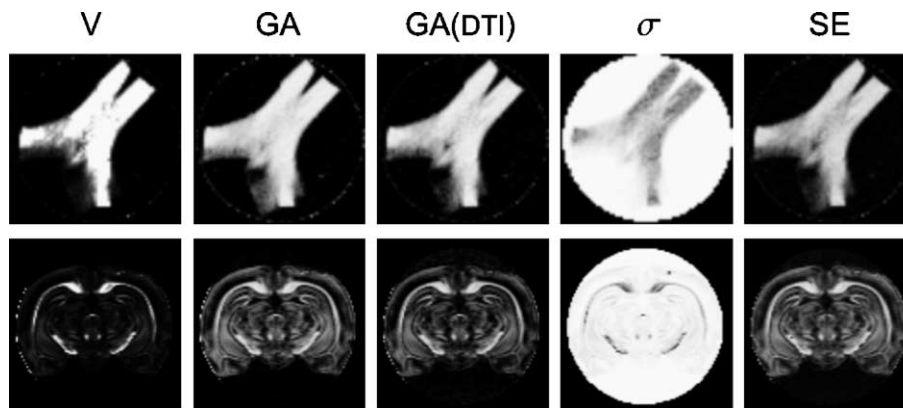Fig. 6. The LS coefficients of the probability profile up to $l = 4$ computed from the excised rat brain data set.

Fig. 7. From left to right: variance, GA, GA from the rank-2 tensor, entropy and SE images calculated for excised rat optic chiasm (top) and brain (bottom) samples.

one another to reach their respective contralateral optic tracts. These orientation maps are consistent with the work by Lessell (1977).

Fig. 9 shows the displacement probabilities calculated from excised coronal rat brain MRI data. At the top left is a diffusion-weighted image that shows the selected ROI. This region is expanded in the large image and depicts the orientations of the highly anisotropic and coherent fibers of the external capsule and corpus callosum bordered inferiorly by the hippocampus and superiorly by radial cortical trajectories. Note, voxels with crossing orientations located superiorly to the external capsule represent the interdigitation of fibers entering the cortex from the external capsule and the corpus callosum into the radial orientations of the cortex. Future investigations employing this method should improve our understanding of normal and pathologically altered neuroanatomy in regions of complex fiber architecture such as the rat brainstem (Fig. 10).

Finally, we show the probability maps computed from excised spinal cord data in Fig. 11. Again, the ROI is specified on a diffusion-weighted image shown on the top left section. The corresponding orientation maps are depicted in the top right panel. Selected pixels of this image were enlarged on the bottom panels of the figure. To demonstrate the shapes more clearly, seven selected surfaces were rotated by $-90°$ about the x axis so that the up-and-down direction in the individual surfaces shown in blue corresponds to the in-and-out direction in red images. The magnified surfaces may represent locations where ventral root fibers from α-motor neurons cross white matter to enter the gray matter of the spinal cord.

Discussion

Exponential attenuation assumption

We have assumed so far that the signal attenuation along each radial line in q-space is characterized by a monoexponential decay. Therefore, it was possible to extract orientational information from data acquired on a single spherical shell and at the origin of the q-space. We would like to note that this is the very assumption intrinsic to DTI, establishing the correspondence between the diffusion tensor and the assumed Gaussian PDF whose orientational mode is estimated from the principal eigenvector of the diffusion tensor. The satisfac-

tory performance of DTI in systems with single fiber orientations has prompted us to keep the monoexponentiality assumption for the radial behavior while complicating the angular structure; this results in non-Gaussian probability profiles. This assumption worked both with our simulations and with real data sets.

In Fig. 12, we show simulated signal values from a one fiber system with a fiber radius of 10 μm when the angle between the fiber orientation and the signal values was assumed by the exponentiality assumption when the experiment is performed at $b = 1500$ s/mm². Note that this is a logarithmic plot, therefore the true deviations between the real and assumed signal values are much smaller than what they appear on the right side of the plot when the signal values are small. Because the q-space is the frequency space for the probabilities, from a signal processing point-of-view, the exponentiality assumption can be thought of as a low-pass filtering of the true probability values. Therefore, the result is a broadened PDF. The computed PDF $P(\mathbf{R})$ can be related to the true PDF $P(\mathbf{R})$ through a convolution with the kernel $\bar{\varepsilon}(\mathbf{R})$, which is the Fourier transform of the function $E(q_1, \mathbf{u})^{q^2/q_1^2} E(q, \mathbf{u})^{-1}$. Here, $E(q_1, \mathbf{u})$ is the HARDI signal attenuation at a b-value corresponding to a q-value of q_1, and $E(q, \mathbf{u})$ is the full q-space signal attenuation function.

In order to demonstrate the effect of the monoexponential signal decay assumption, we performed rigorous simulations of high resolution q-space experiments. In these simulations, signal attenuation values were computed on a 128^3 Cartesian q-space grid, yielding a resolution of $(0.5 \ \mu m)^3$ in the displacement space. Signal decay values were transformed to the displacement probabilities via a fast Fourier transform (FFT). Later, isoprobability surfaces of the probability maps were computed and the resulting surfaces were sharpened by subtracting the minimum probability value. Next, the surfaces were expanded to cover a large region of the designated space to exaggerate the orientational structure of these surfaces. The same procedure was applied to the signal values as assumed by the HARDI experiment with monoexponential signal attenuation assumption and the effective kernel that causes the broadening of the probability maps. Note that in this scheme both the transform (between the signal and probability domains) and the surfaces to be visualized are different from the DOT analysis. The results for simulated one- and two-fiber voxels are provided in Fig. 13a where the signal decays were computed using Eq. (22) as
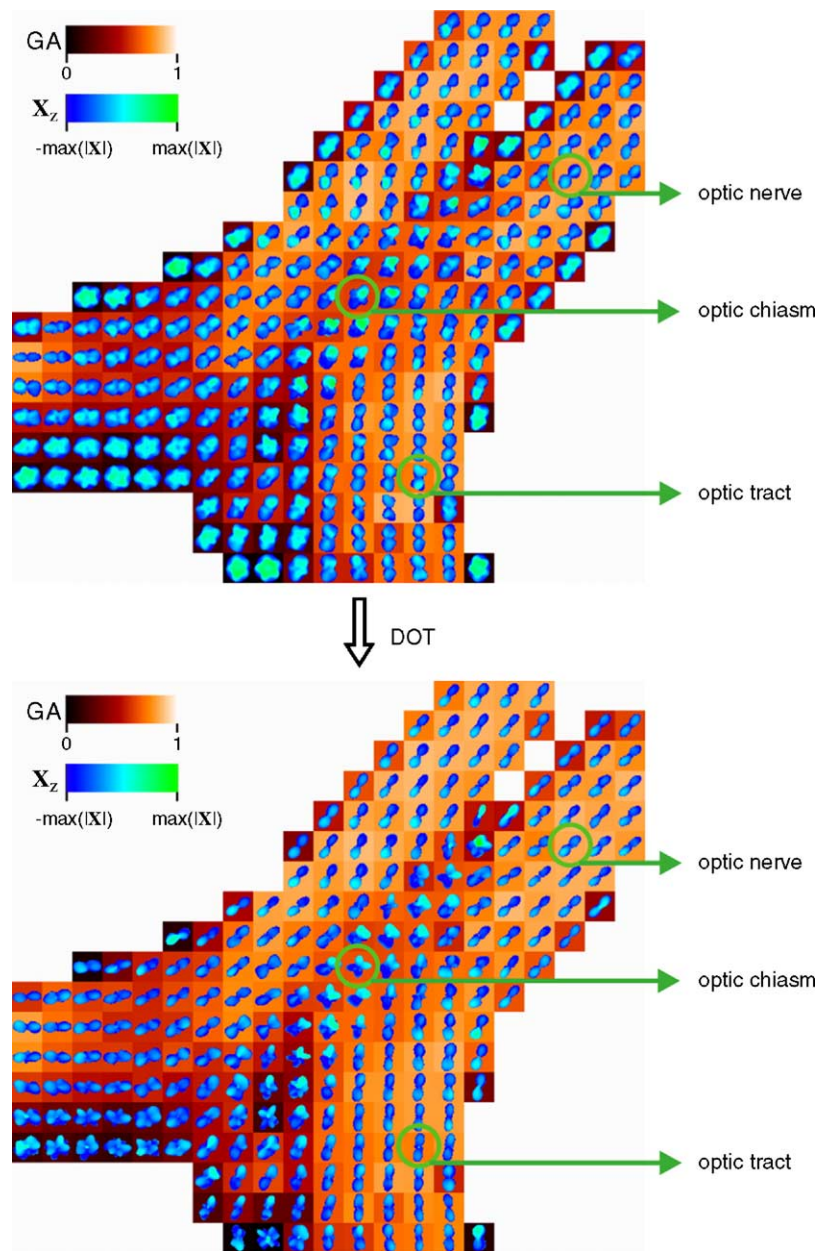
Fig. 8. Diffusivity profiles (top) and probability maps (bottom) computed from a rat optic chiasm data set overlaid on axially oriented GA maps. The decussations of myelinated axons from the two optic nerves at the center of the optic chiasm are readily apparent using the DOT method. These crossing fibers carry information from the temporal visual fields to the contralateral cerebral hemispheres. In Figs. 8–11, the orientation surfaces are color-coded such that portions of the surfaces pointing towards or away from the reader are green and blue respectively (see inset).

before. In these simulations, the water molecules are trapped inside the bounding cylinders, therefore the signal attenuation is clearly not monoexponential even when there is only one fiber. In both cases, one gets slightly anisotropic convolution kernels[2] that give rise to some broadening of the computed probability profiles without creating a realizable change in the peaks of the isosurfaces. This may aid in understanding why it was possible to map the fiber orientations accurately in the simulations (see Table 1) under the assumption that the signal decays mono-exponentially along each direction. Note that the nature of the

convolution kernel in the one-fiber system also justifies the performance of DTI in producing correct fiber orientations in the presence of restricted diffusion.

The same simulations were repeated under the assumption that, in each fiber population, the diffusion process is Gaussian and can be modeled using a diffusion tensor with axial symmetry, where the ratio of the diffusivity along the fiber axis to those along directions perpendicular to it is 8. Although this is a less realistic model for diffusion taking place within fibrous tissues, it provides an independent test for the assumption we have employed. The results are provided in Fig. 13b. As expected, the convolution kernel is just a delta function when there is only one Gaussian which is a consequence of the fact

---

[2] Note that the sharpening and expansion of the isosurfaces overemphasize the anisotropy of the convolution kernels significantly.
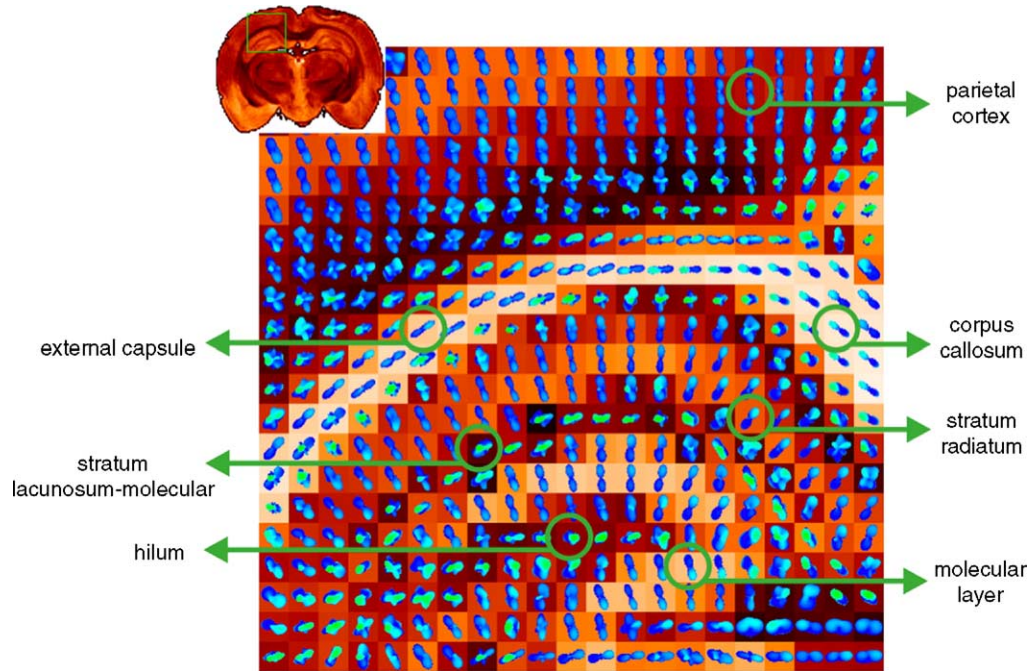
Fig. 9. Probability map of a coronally oriented GA image of the rat brain. Diffusion fiber orientations in the parietal cortex were collinear with the apical dendrites and axons of cortical pyramidal neurons found in cortical layers III–V. In the dorsal hippocampus, the molecular layer and stratum radiatum fiber orientations paralleled the apical dendrites of granule cells and pyramidal neurons respectively, whereas in the stratum lacunosum, moleculare orientations paralleled Schaffer collaterals from CA1 neurons and perforant fibers from the entorhinal cortex.

that MR signal is truly monoexponential in this case. In the case of two orientations, the convolution kernel is slightly anisotropic and very local resulting in a minor blurring of the probability maps. The sharpened isosurfaces clearly demonstrate that the peaks of the isosurfaces are not altered.

Avoiding some kind of deviation from the true probability values seems impossible when the reconstruction is performed from limited samples of q-space (e.g. HARDI experiments). However, when data points are collected from a greater region in q-space (such as on several concentric shells), the DOT method
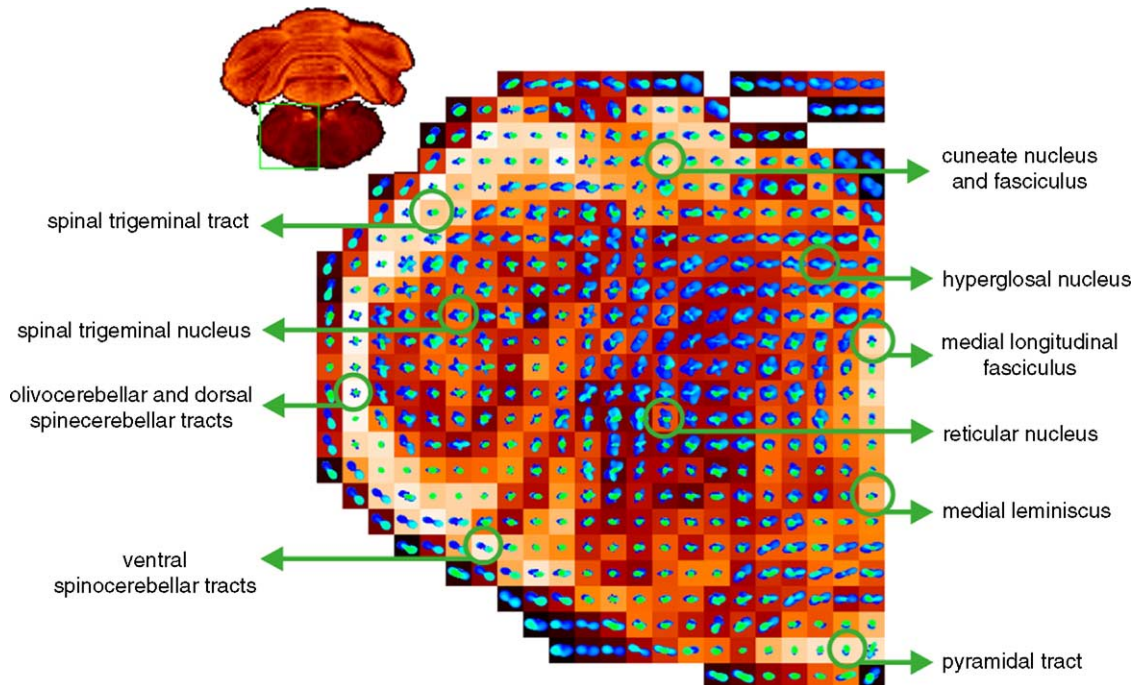

Fig. 10. The diffusion orientation transform (DOT) described in this paper also characterized the complex cytoarchitecture of the rat brainstem well as shown in this probability map from one side of the rat medulla.
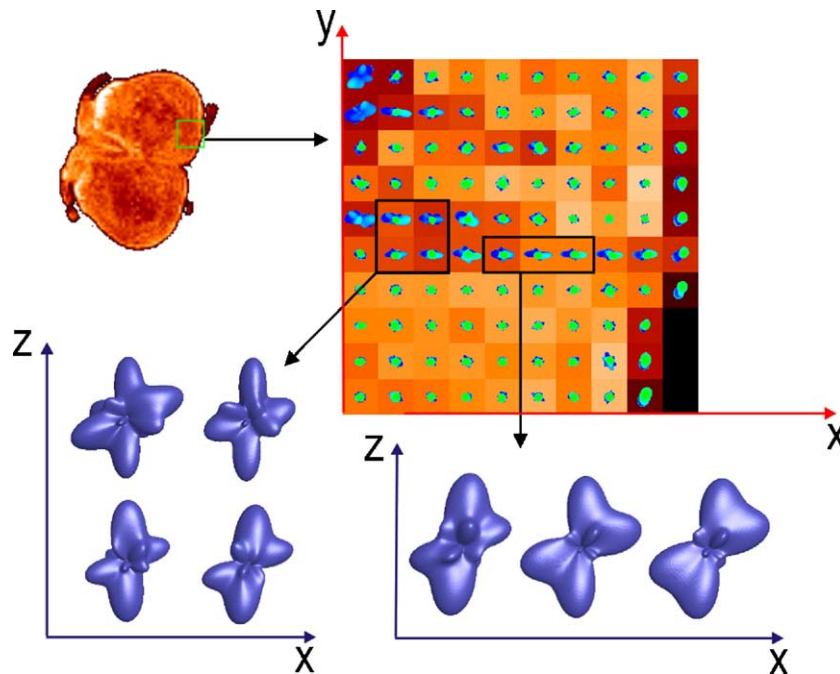
Fig. 11. Probability maps calculated from a diffusion-weighted data set acquired from an excised rat spinal cord. The surfaces in the bottom row depict the probability profiles selected from the image matrix and rotated −90° about the x axis. These crossing fiber orientations may represent coherent ventral root spinal nerve fibers penetrating along the x axis perpendicular to ascending and descending white matter axons in the anterior funiculus to reach the anterior horn motor neurons.

provides a unique opportunity to significantly and efficiently reduce the broadening mentioned above. This scheme is described in the next section.

Another case in which the monoexponential signal decay assumption may fail is when "diffraction" effects are present, giving rise to non-monotonic dependence of the signal values on the gradient strength (Callaghan et al., 1991). This effect is observed in the presence of a great deal of periodicity and therefore is unlikely to be observed when there are heterogeneities in the fiber orientations. Avram et al. (2004) have reported that in coherent cylinders the diffraction-like effects are
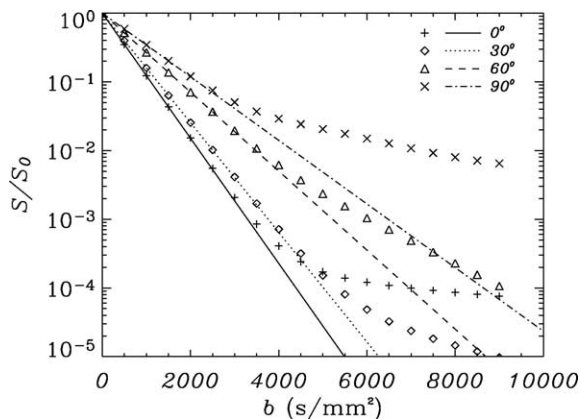

Fig. 12. Logarithmic plot of the signal attenuation values as a function of the b-value. The symbols indicate the signal attenuations calculated from a simulation of a single fiber system, while the lines indicate the monoexponential fits when the HARDI experiment is performed at a b-value of 1500 s/mm². The curves correspond to different angles between the diffusion gradient and fiber orientations.

observed experimentally when the diffusion gradients are oriented almost perpendicular to the fiber axis. In a HARDI experiment, this may cause some problems since the signal values perpendicular to the fiber axis will be quite sensitive to the selection of the b-value.

We also have investigated the effect of b-value on the constructed probability surfaces. To this end, we simulated HARDI experiments performed at increasing b-values on 1- and 2-fiber systems. We also repeated the simulations for fibers of radii 5 and 10 μm. The selected results are provided in Fig. 14. The most reassuring finding is that there has been no realizable alteration in the peaks of the distributions indicating that the calculated fiber orientations are robust to the choice of b-value. However, it is evident that the probability surfaces are sharper and multiple orientations are better resolved at higher b-values. As we have demonstrated before, a b-value of 1500 s/mm² seems sufficient to resolve the fiber crossings when the radii of the fibers are 5 μm. However, when the radii are doubled, it is advantageous to collect the data at higher b-values. It should be noted that spurious peaks start to develop at very high b-values (see the first two rows of the last column). This may be explained by the crossing of the signal decay curves in Fig. 12, which suggests that at high b-values the order of signal values from different orientations may be altered.

Extension to multiexponential attenuation

We have thus far employed the monoexponentiality assumption of the signal attenuation. However, the same formalism provides a surprisingly simple extension to multiexponential attenuation, which has been shown in numerous articles to provide a very accurate characterization of the radial behavior (in q-space) of the MR data collected from tissue (e.g. Niendorf et al., 1996).
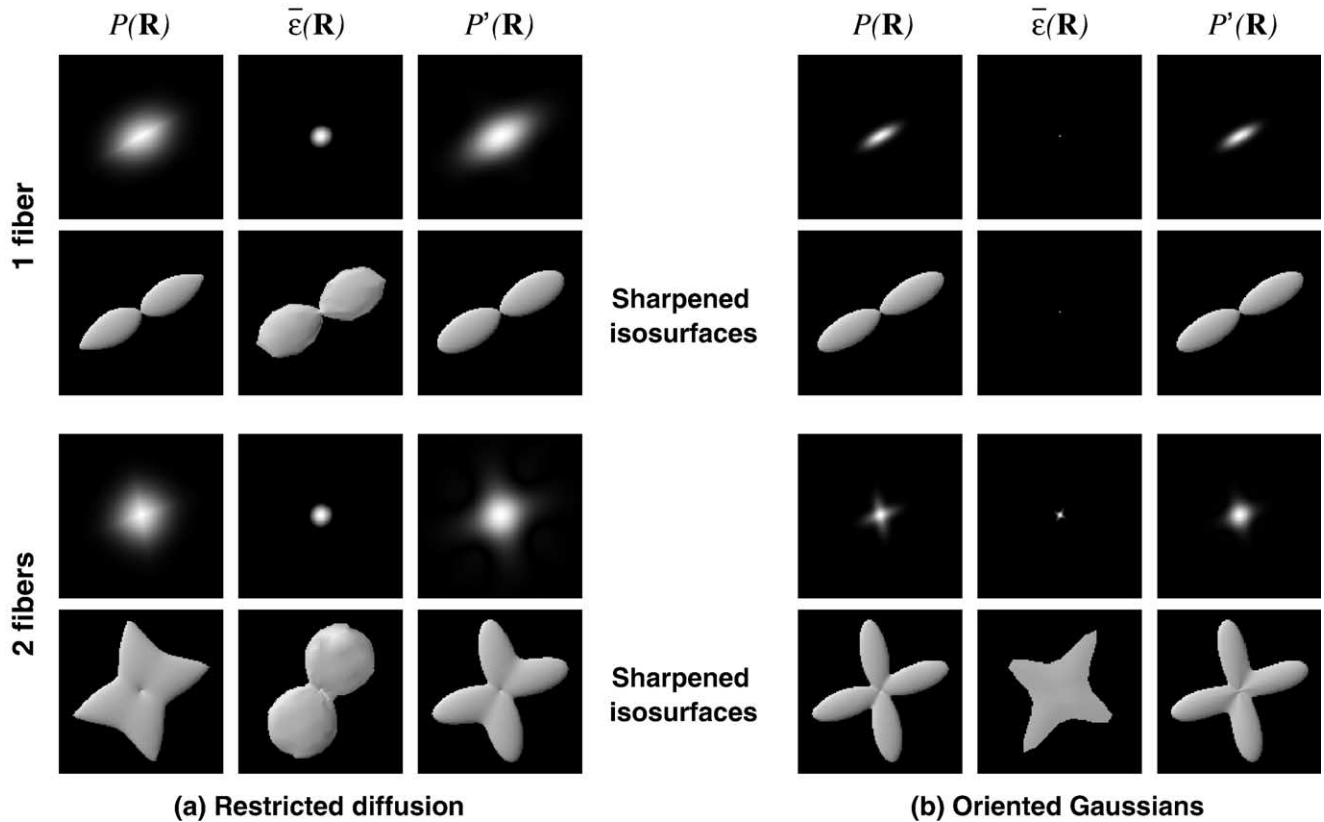
Fig. 13. Simulations of single (top two rows) and two-fiber (bottom two rows) systems. (a) The signal values were computed using Eq. (22). The first column shows the water displacement probability maps that would be obtained from a rigorous three-dimensional q-space measurement and the employment of an FFT. The second column depicts the convolution kernels that are induced by the monoexponentiality assumption. The resulting probability maps, which can be obtained either by employing the monoexponential attenuation assumption and taking an FFT or convolving the function in the first column with the kernel in the second, are shown in the third column. The isosurfaces of the three-dimensional maps were sharpened and expanded to clarify the orientational appearance of the corresponding maps. (b) The same images were provided for signal profiles generated from oriented Gaussians. Evidently, the employment of the monoexponential attenuation assumption broadens the probability maps without significantly altering its orientational features. Note that the sharpening of the isosurfaces exaggerates the directional dependence of the associated smoothing kernels.

To derive the correct generalization, we start by replacing the Stejskal–Tanner Eq. (2) with the expression:

$$E(b, \boldsymbol{u}) = \sum_{i}^{N_E} f_i(\boldsymbol{u}) e^{-bD_i(\boldsymbol{u})}, \tag{23}$$

where N_E is the number of terms (exponentials, transients) in the series, $D_i(\boldsymbol{u})$ is the i-th diffusion coefficient for the gradient direction $\boldsymbol{u}$ and $f_i(\boldsymbol{u})$ is the "volume fraction" of the i-th exponential satisfying the relationship

$$\sum_{i}^{N_E} f_i(\boldsymbol{u}) = 1 \tag{24}$$

Carrying out the same algebra as before, Eqs. (5) and (14) hold with the definition

$$I_l(\boldsymbol{u}) = \sum_{i}^{N_E} f_i(\boldsymbol{u}) I_{li}(\boldsymbol{u}) \tag{25}$$

where

$$I_{li}(\boldsymbol{u}) = 4\pi \int_0^\infty dq \, q^2 \, j_l(2\pi q R_0) \, \exp\left(-4\pi^2 q^2 t D_i(\boldsymbol{u})\right), \tag{26}$$

which is the same expression when $D(\boldsymbol{u})$ in Eq. (6) is replaced by $D_i(\boldsymbol{u})$. Therefore, either of the forms given in Eqs. (27) or (28) can still be used to calculate $I_{li}(\boldsymbol{u})$ from $D_i(\boldsymbol{u})$.

The extension to multiexponential attenuation requires the following modifications for the implementation of the DOT:

(1) Fit multiexponential function Eq. (23) along each radial line in q-space to estimate $f_i(\boldsymbol{u})$ and $D_i(\boldsymbol{u})$.
(2) For each diffusion coefficient $D_i(\boldsymbol{u})$ corresponding to each term in the series, calculate $I_{li}(\boldsymbol{u})$ from Eq. (26).
(3) Calculate $I_l(\boldsymbol{u})$ from Eq. (25).
(4) Apply either the parametric or nonparametric reconstruction as before.

Fig. 15 shows the biexponential fits to the data points already presented in Fig. 12. The improvement in the functional fits is evident. We would like to stress that we utilize the multiexponential fit solely to provide an approximation and extrapolation to the signal attenuation and by no means do we intend to make inferences about the compartmentation in tissue from this fit. In other words, we exploit the performance of multiexponential fits realized in studies involving compartmentation to improve on the orientation mapping results that are achieved using the DOT technique.
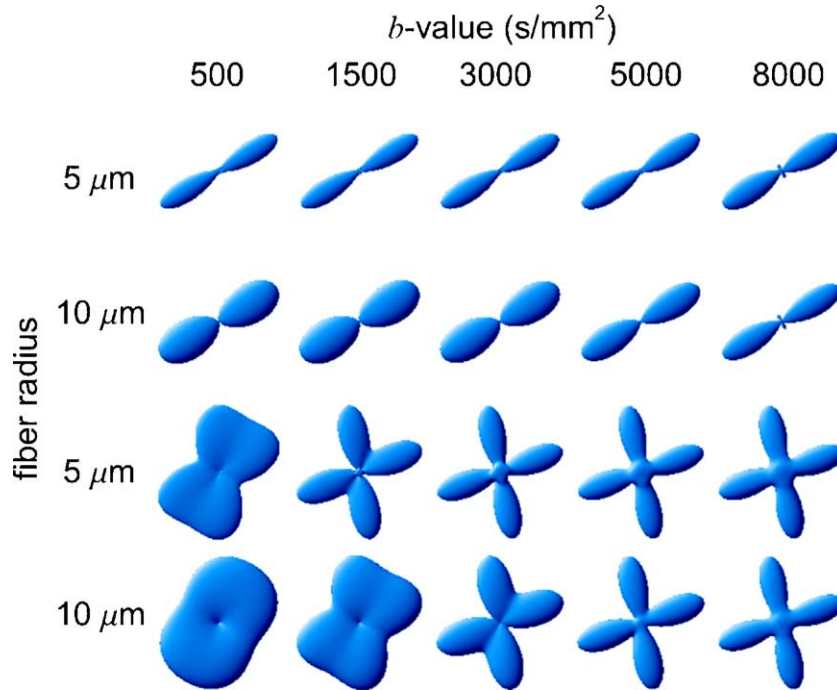
Fig. 14. Simulations of 1- and 2-fiber systems as a function of b-value where the radii of the fibers were taken to be 5 and 10 μm.

We have tested the proposed extension scheme on our simulated data from 1-, 2- and 3-fiber systems. The results are shown in Fig. 16. It is clear that the monoexponential and multiexponential fits provide the same orientational information, yet the constructed probability surfaces in the latter case resolve the distinct fiber orientations better, most notably in the 3-fiber system. However, the results indicate that transition from bi- to triexponential fits does not result in a significant improvement. This demonstrates the sufficient accuracy of the biexponential fits to the signal attenuation values.

Unfortunately, using a biexponential attenuation fit in our formalism would necessitate collecting about three times the number of data points when compared with the case in which the mono-exponentiality assumption is made. This is because there are $2 \times N_E$ unknowns in the fit, and if one chooses to collect data at $b = 0$, then

at least $2 \times N_E - 1$ spherical shells have to be sampled for the N_E exponential fits.

Conclusion

The DOT technique provides a direct estimation of displacement probability surfaces within each voxel from multi-orientational diffusion-weighted MRI data. The method is robust and fast. DOT can be implemented nonparametrically for direct estimation of probability values along desired directions or by using an SHT that gives the Laplace series coefficients of the probability profile. In either case, high resolution probability surfaces can be reconstructed easily from the signal values. Furthermore, the behavior of the MR signal intensities with increasing b-values can be characterized by mono- or multiexponential fits. Our findings indicate that multiexponential fits result in improved reconstructions. However, when the acquisition time or the available gradient strength is limited, the monoexponentiality assumption can be employed. This results in some broadening of the PDF whose angular structure is smoother. As demonstrated in excised rat nervous tissue, the potential applications of our approach include more accurate estimates of fiber orientations that will improve the existing fiber tractography schemes. This then could enable the reliable mapping of more connections between different parts of fibrous tissues.
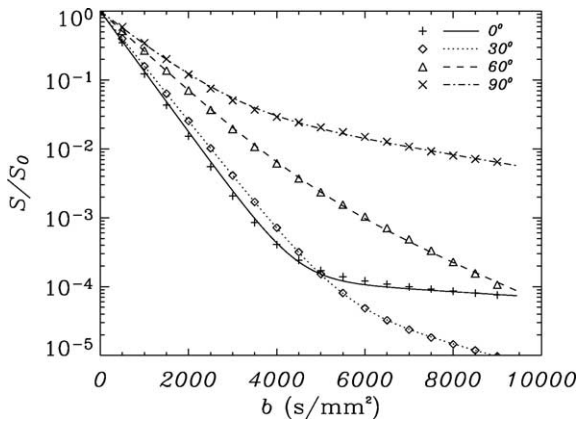

Fig. 15. The symbols indicate the signal attenuations calculated for the same system as in Fig. 12, whereas the lines indicate the curves obtained from a biexponential fit to these data points. The curves correspond to different angles between the diffusion gradient and fiber orientations.
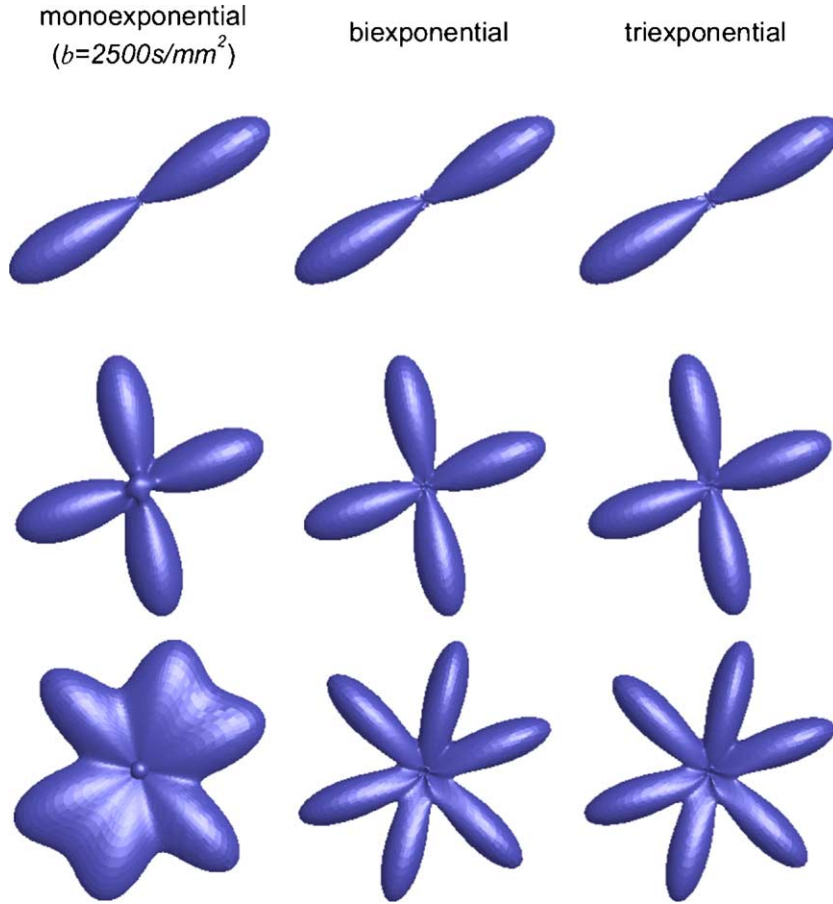
Fig. 16. Simulations of 1-, 2- and 3-fiber systems with mono- ($b = 2500$ s/mm^2), bi- and triexponential fits (from data up to $b = 9000$ s/mm^2). Similar to Fig. 1, the orientations of the simulated fibers are specified by the azimuthal angles $\phi_1 = 30°$, $\phi_2 = \{20°, 100°\}$ and $\phi_3 = \{20°, 75°, 135°\}$ for the 1-, 2- and 3-fiber systems respectively. All fibers lie on the image plane.

the National High Magnetic Field Laboratory (NHMFL), Tallahassee.

Appendix A. The radial integral

The integral in Eq. (6) can be evaluated and it is given by

$$
I_l(\boldsymbol{u}) = \frac{R_0^l \Gamma\left(\frac{l+3}{2}\right)}{2^{l+3} \pi^{3/2} (D(\boldsymbol{u})t)^{(l+3)/2} \Gamma(l+3/2)}
$$
$$
\times {}_1F_1\left(\frac{l+3}{2}; l+\frac{3}{2}; -\frac{R_0^2}{4D(\boldsymbol{u})t}\right), \tag{27}
$$

where ${}_1F_1$ is the confluent hypergeometric function of the first kind (see Appendix B). Using the recurrence relations of the confluent hypergeometric functions provided in Eq. (31) iteratively, these functions can be written as the sum of two terms, one of them being proportional to ${}_1F_1\left(\frac{1}{2}; \frac{3}{2}; -\frac{R_0^2}{4D(\boldsymbol{u})t}\right)$ where the other term will be proportional to ${}_1F_1\left(\frac{3}{2}; \frac{3}{2}; -\frac{R_0^2}{4D(\boldsymbol{u})t}\right)$. Using Eqs. (32) and (33), it can be seen that these functions are proportional to the error function and Gaussian respectively.

Therefore, the resulting expression is given by

$$
I_l(\boldsymbol{u}) = A_l(\boldsymbol{u}) \frac{\exp\left(-\beta(\boldsymbol{u})^2/4\right)}{(4\pi D(\boldsymbol{u})t)^{3/2}} + B_l(\boldsymbol{u}) \frac{\mathrm{erf}(\beta(\boldsymbol{u})/2)}{4\pi R_0^3}, \tag{28}
$$

where

$$
\beta(\boldsymbol{u}) = \frac{R_0}{\sqrt{D(\boldsymbol{u})t}}. \tag{29}
$$

$A_l(\boldsymbol{u})$ and $B_l(\boldsymbol{u})$ functions up to $l = 8$ are given in Table 2. Note that, throughout the paper, only the even-order terms are included as a consequence of the antipodal symmetry of the diffusivity profiles as well as displacement PDFs. The derivation of the particular forms for the $A_l(\boldsymbol{u})$ and $B_l(\boldsymbol{u})$ for arbitrary (even) values of l is provided in Appendix C.

Table 2
$A_l(\boldsymbol{u})$ and $B_l(\boldsymbol{u})$ functions up to $l = 8$

l	$A_l(\boldsymbol{u})$	$B_l(\boldsymbol{u})$
0	1	0
2	$-(1 + 6\beta^{-2})$	3
4	$1 + 20\beta^{-2} + 210\beta^{-4}$	$15/2\ (1-14\beta^{-2})$
6	$-(1 + 42\beta^{-2} + 1575/2$ $\beta^{-4} + 10,395\beta^{-6})$	$105/8\ (1-36\beta^{-2} + 396\beta^{-4})$
8	$1 + 72\beta^{-2} + 10,395/4$ $\beta^{-4} + 45,045\beta^{-6}+675,675\beta^{-8}$	$315/16\ (1-66\beta^{-2} +$ $1716\beta^{-4} - 17,160\beta^{-6})$

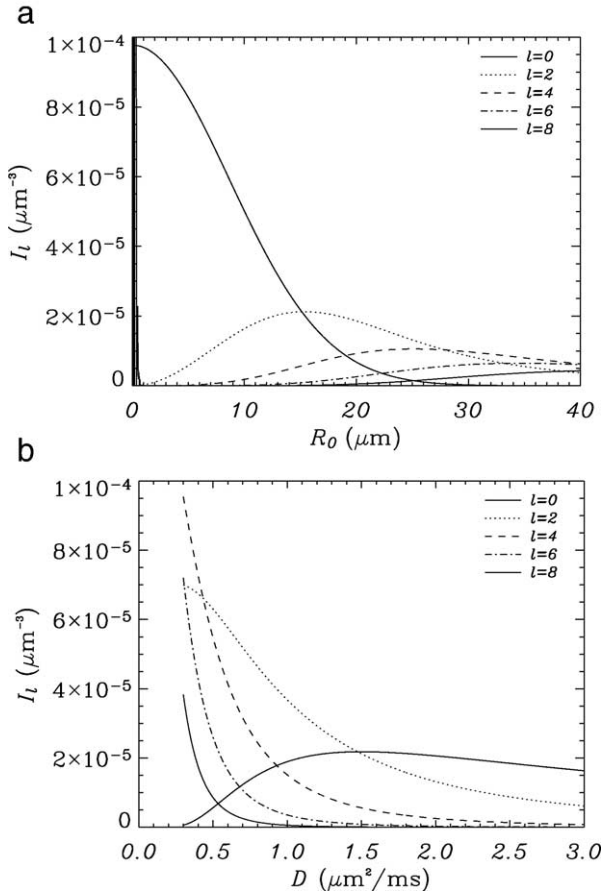In this table, β stands for $\beta(\boldsymbol{u})$.

Fig. 17. Dependence of the radial integral I_l on R_0 (top) and on diffusivity (bottom). The curves are drawn for l values ranging from 0 to 8.

In Fig. 17a, we plot the I_l values as a function of R_0 calculated with double precision using Eq. (28) where $D = 1.5 \times 10^{-3}$ mm^2/s and $t = 25$ ms. Very large values taken by the higher-order terms near the origin are due to round-off and errors. However, this is not a big concern because we will be mostly interested in the values of this function in the 10–20 μm range. Note that the contribution from higher-order terms is rapidly collapsing for R_0 values in this range. Shown in Fig. 17b are the curves generated by keeping R_0 fixed at the value of 15 μm and varying the diffusion coefficients between 3×10^{-4} and 3×10^{-3} mm^2/s. This plot indicates the nontrivial manner in which an angular diffusivity profile influences the I_l and hence the probability values.

Appendix B. Confluent hypergeometric functions of the first kind

The confluent hypergeometric function of the first kind (also known as Kummer's function of the first kind or Kummer's function) $_1F_1(a; b; x)$ is given by the series (Abramowitz and Stegun, 1977)

$$_1F_1(a; b; x) = \sum_{k=0}^{\infty} \frac{(a)_k x^k}{(b)_k k!}, \tag{30}$$

where $(a)_k = a(a + 1)(a + 2) \dots (a + k - 1)$ with $(a)_0 = 1$.

Among others, the confluent hypergeometric function of the first kind satisfies the recurrence relations

$$(b - a)_1F_1(a - 1; b; x) + (2a - b + x)_1F_1(a; b; x)$$
$$- a_1F_1(a + 1; b; x) = 0$$

$$b(b - 1)_1F_1(a; b - 1; x) + b(1 - b - x)_1F_1(a; b; x)$$
$$+ x(b - a)_1F_1(a; b + 1; x) = 0$$

$$(1 + a - b)_1F_1(a; b; x) - a_1F_1(a + 1; b; x)$$
$$+ (b - 1)_1F_1(a; b - 1; x) = 0. \tag{31}$$

Many of the commonly used functions are special instances of the confluent hypergeometric function of the first kind. For example,

$$_1F_1(a; a; x) = e^x \tag{32}$$

$$_1F_1\left(\frac{1}{2}; \frac{3}{2}; -x^2\right) = \frac{\pi^{1/2}}{2x} \text{erf}(x). \tag{33}$$

Finally, the asymptotic behavior of the function $_1F_1(a; b; x)$ as $|x| \to \infty$ when x is real, is given by

$$\frac{_1F_1(a; b; x)}{\Gamma(b)}$$

$$= \frac{e^{i\pi a} x^{-a}}{\Gamma(b - a)} \left[\sum_{n=0}^{V-1} \frac{(a)_n (1 + a - b)_n}{n!} (-x)^{-n} + O\left(|x|^{-V}\right) \right]$$

$$+ \frac{e^x x^{a-b}}{\Gamma(a)} \left[\sum_{n=0}^{W-1} \frac{(b - a)_n (1 - a)_n}{n!} -x^{-n} + O\left(|x|^{-W}\right) \right], \tag{34}$$

where V and W are the number of terms kept in the first and second series respectively.

Appendix C. A_l and B_l coefficients

Although the recursion relations of the confluent hypergeometric functions provided in Eq. (31) are useful in seeing that the $I_l(\boldsymbol{u})$ functions can be expressed as the sum of two terms (one involving exponential and the other involving error functions as in Eq. (28)), the derivation of the analytical form of the A_l and B_l coefficients using these recursion relations is a formidable task. Therefore, in order to find analytical expressions for the A_l and B_l coefficients for a general l value, we make a term-by-term comparison of the asymptotic form of the I_l function evaluated from Eq. (34) with the asymptotic form of Eq. (28). After some tedious algebra, we have found that, if A_{ln} and B_{ln} are defined such that

$$A_l(\boldsymbol{u}) = \sum_{n=0}^{l/2} A_{\ln}\beta(\boldsymbol{u})^{-2n} \text{ and } B_l(\boldsymbol{u}) = \sum_{n=0}^{l/2-1} B_{\ln}\beta(\boldsymbol{u})^{-2n}, \tag{35}$$

the following expressions hold:

$$A_{\ln} = \begin{cases} A^0 & \text{, if } n < 2 \\ A^0 + \sum_{t=1}^{n-1} \dfrac{(-1)^{t-1}(2t-3)!!\left(\frac{l+3}{2}\right)_{n-t-1}\left(1-\frac{l}{2}\right)_{n-t-1}(l+1)!!}{\Gamma(l/2)(n-t-1)!2^{l/2-2n+t}} & \text{, if } n \geq 2 \end{cases} \tag{36}$$

where $(l+1)!! = (l+1)(l-1)\ldots 1$ and

$$A^0 = \frac{(-1)^{l/2+n}}{n!}2^{2n}\left(\frac{l}{2}\right)_n\left(-\frac{l}{2}-\frac{1}{2}\right)_n \tag{37}$$

and

$$B_{\ln} = \frac{\left(\frac{l+3}{2}\right)_n\left(1-\frac{l}{2}\right)_n(l+1)!!}{\Gamma\left(\frac{l}{2}\right)n!2^{l/2-1-2n}}. \tag{38}$$

We have verified using Mathematica that these expressions indeed yield the correct coefficients for the $I_l(\boldsymbol{u})$ functions.

Appendix D. Convergence of the Laplace series for the probability profile

Theorem. *The series given by* (see Eq. (5))

$$P(R_0\boldsymbol{r}) = \sum_{l=0}^{\infty}\sum_{m=-l}^{l}(-i)^l Y_{lm}(\boldsymbol{r})\int d\boldsymbol{u}Y_{lm}(\boldsymbol{u})^*I_l(\boldsymbol{u}) \tag{39}$$

is convergent.

Proof. We start by inserting the upper bound for the spherical Bessel functions of order l (Abramowitz and Stegun, 1977)

$$|j_l(2\pi qR_0)| \leq \frac{\sqrt{\pi}(\pi qR_0)^l}{2\Gamma\left(l+\frac{3}{2}\right)} = \frac{(2\pi qR_0)^l}{(2l+1)!!} \tag{40}$$

into Eq. (6). This yields the upper bound for the functions $I_l(\boldsymbol{u})$

$$I_l(\boldsymbol{u}) \leq \frac{(l+1)!!}{(2l+1)!!2^{l/2}(4\pi D(\boldsymbol{u})t)^{3/2}}\left(\frac{R_0^2}{D(\boldsymbol{u})t}\right)^{l/2}. \tag{41}$$

Note that using the addition theorem for spherical harmonics (Arfken and Weber, 2001),

$$\sum_{m=-l}^{l}Y_{lm}(\boldsymbol{r})Y_{lm}(\boldsymbol{u})^* = \frac{2l+1}{4\pi}P_l(\boldsymbol{u}\boldsymbol{r}), \tag{42}$$

where $P_l(x)$ is the l-th order Legendre polynomial, it is possible to express Eq. (39) in the following form:

$$P(R_0\boldsymbol{r}) = \sum_{l=0}^{\infty}\varrho_l, \tag{43}$$

where

$$\varrho_l = \frac{(-i)^l(2l+1)}{4\pi}\int d\boldsymbol{u}I_l(\boldsymbol{u})P_l(\boldsymbol{u}\boldsymbol{r}). \tag{44}$$

Using the generating function for the Legendre polynomials, it is possible to prove that (Arfken and Weber, 2001)

$$P_l(\cos\gamma) \leq 1. \tag{45}$$

Using Eqs. (41) and (45), it is easy to see that

$$|\varrho_l| \leq \frac{(l+1)!!}{(2l-1)!!2^{l/2}(4\pi D_{\min}t)^{3/2}}\left(\frac{R_0^2}{D_{\min}t}\right)^{l/2} = \xi_l, \tag{46}$$

where $D_{\min} = \min D(\boldsymbol{u})$. Note that

$$\lim_{l\to\infty}\frac{\xi_{l+2}}{\xi_l} = \lim_{l\to\infty}\frac{l+3}{(2l+1)(2l+3)}\frac{R_0^2}{2D_{\min}t} = 0. \tag{47}$$

Therefore, using the d'Alembert (Cauchy) ratio test, the series $\sum_{l=0}^{\infty}\xi_l$ converges. Using the comparison test, it is straightforward to see that the series $\sum_{l=0}^{\infty}|\varrho_l|$ converges since $0 \leq |\varrho_l| \leq \xi_l$. Therefore, the series in Eq. (39) is absolutely convergent. □

References

Abramowitz, M., Stegun, I.A., 1977. Handbook of Mathematical Functions: With Formulas, Graphs, and Mathematical Tables. Dover Publications, New York.

Alexander, D.C., Barker, G.J., Arridge, S.R., 2002. Detection and modeling of non-Gaussian apparent diffusion coefficient profiles in human brain data. Magn. Reson. Med. 48 (2), 331–340.

Arfken, G.B., Weber, H.J., 2001. Mathematical Methods for Physicists. Academic Press, San Diego.

Assaf, Y., Freidlin, R.Z., Rohde, G.K., Basser, P.J., 2004. New modeling and experimental framework to characterize hindered

and restricted water diffusion in brain white matter. Magn. Reson. Med. 52 (5), 965–978.

Avram, L., Assaf, Y., Cohen, Y., 2004. The effect of rotational angle and experimental parameters on the diffraction patterns and microstructural information obtained from q-space diffusion NMR: implication for diffusion in white matter fibers. J. Magn. Reson. 169 (1), 30–38.

Basser, P.J., 1995. Inferring microstructural features and the physiological state of tissues from diffusion-weighted images. NMR Biomed. 8 (7–8), 333–344.

Basser, P.J., 2002. Relationships between diffusion tensor and q-space MRI. Magn. Reson. Med. 47, 392–397.

Basser, P.J., Mattiello, J., LeBihan, D., 1994. Estimation of the effective self-diffusion tensor from the NMR spin echo. J. Magn. Reson., B 103 (3), 247–254.

Basser, P.J., Mattiello, J., LeBihan, D., 1994. MR diffusion tensor spectroscopy and imaging. Biophys. J. 66 (1), 259–267.

Basser, P.J., Pajevic, S., Pierpaoli, C., Duda, J., Aldroubi, A., 2000. In vivo fiber tractography using DT-MRI data. Magn. Reson. Med. 44, 625–632.

Callaghan, P.T., 1991. Principles of Nuclear Magnetic Resonance Microscopy. Clarendon Press, Oxford.

Callaghan, P.T., Coy, A., MacGowan, D., Packer, K.J., Zelaya, F.O., 1991. Diffraction-like effects in NMR diffusion studies of fluids in porous solids. Nature 351, 467–469.

Chenevert, T.L., Brunberg, J.A., Pipe, J.G., 1990. Anisotropic diffusion in human white matter: demonstration with MR techniques in vivo. Radiology 177 (2), 328–329.

Cleveland, G.G., Chang, D.C., Hazlewood, C.F., Rorschach, H.E., 1976. Nuclear magnetic resonance measurement of skeletal muscle: anisotropy of the diffusion coefficient of the intracellular water. Biophys. J. 16 (9), 1043–1053.

Conturo, T.E., Lori, N.F., Cull, T.S., Akbudak, E., Snyder, A.Z., Shimony, J.S., McKinstry, R.C., Burton, H., Raichle, M.E., 1999. Tracking neuronal fiber pathways in the living human brain. Proc. Natl. Acad. Sci. 96, 10422–10427.

Frank, L.R., 2002. Characterization of anisotropy in high angular resolution diffusion-weighted MRI. Magn. Reson. Med. 47 (6), 1083–1099.

Inglis, B.A., Bossart, E.L., Buckley, D.L., Wirth, E.D., Mareci, T.H., 2001. Visualization of neural tissue water compartments using biexponential diffusion tensor MRI. Magn. Reson. Med. 45 (4), 580–587.

Jansons, K.M., Alexander, D.C., 2003. Persistent angular structure: new insights from diffusion magnetic resonance imaging data. Inverse Problems 19, 1031–1046.

Lessell, S., 1977. The histology and histochemistry of the rat's optic nerve and chiasm. Am. J. Ophthalmol. 84 (5), 681–688.

Liu, C.L., Bammer, R., Moseley, M.E., 2003. Generalized diffusion tensor imaging (GDTI): a method for characterizing and imaging diffusion anisotropy caused by non-Gaussian diffusion. Isr. J. Chem. 43 (1–2), 145–154.

Maier, S.E., Vajapeyam, S., Mamata, H., Westin, C.F., Jolesz, F.A., Mulkern, R.V., 2004. Bioexponential diffusion tensor analysis of human brain diffusion data. Magn. Reson. Med. 51 (2), 321–330.

Mori, S., Crain, B.J., Chacko, V.P., van Zijl, P.C.M., 1999. Three-dimensional tracking of axonal projections in the brain by magnetic resonance imaging. Ann. Neurol. 45, 265–269.

Moseley, M.E., Cohen, Y., Kucharczyk, J., Mintorovitch, J., Asgari, H.S., Wendland, M.F., Tsuruda, J., Norman, D., 1990. Diffusion-weighted MR imaging of anisotropic water diffusion in cat central nervous system. Radiology 176 (2), 439–445.

Niendorf, T., Dijkhuizen, R.M., Norris, D.G., van Lookeren Campagne, M., Nicolay, K., 1996. Biexponential diffusion attenuation in various states of brain tissue: implications for diffusion-weighted imaging. Magn. Reson. Med. 36 (6), 847–857.

Özarslan, E., Mareci, T.H., 2003. Generalized diffusion tensor imaging and analytical relationships between diffusion tensor imaging and high angular resolution diffusion imaging. Magn. Reson. Med. 50, 955–965.

Özarslan, E., Vemuri, B.C., Mareci, T.H., 2004a. Generalized diffusion tensor imaging of excised rat brain. Proc. of the 12th Scientific Meeting of ISMRM, p. 92.

Özarslan, E., Vemuri, B.C., Mareci, T.H., 2004b. Multiple fiber orientations resolved by generalized diffusion tensor imaging. Proc. of the 12th Scientific Meeting of ISMRM, p. 89.

Özarslan, E., Vemuri, B.C., Mareci, T.H., 2005. Generalized scalar measures for diffusion MRI using trace, variance and entropy. Magn. Reson. Med. 53 (4), 866–876.

Pajevic, S., Pierpaoli, C., 1999. Color schemes to represent the orientation of anisotropic tissues from diffusion tensor data: application to white matter fiber tract mapping in the human brain. Magn. Reson. Med. 42 (3), 526–540.

Parker, G.J.M., Alexander, D.C., 2003. Probabilistic Monte Carlo based mapping of cerebral connections utilising whole-brain crossing fibre information. In: Taylor, C.J., Noble, A. (Eds.), Information Processing in Medical Imaging (IPMI'03), Lecture of Notes in Computer Science, vol. 2737. Springer, pp. 242–254.

Ritchie, D.W., Kemp, G.J.L., 1999. Fast computation, rotation, and comparison of low resolution spherical harmonic molecular surfaces. J. Comput. Chem. 20 (4), 383–395.

Schwabl, F., 1989. Quantum Mechanics. Springer-Verlag, Berlin.

Söderman, O., Jönsson, B., 1995. Restricted diffusion in cylindrical geometry. J. Magn. Reson., A (117), 94–97.

Stejskal, E.O., 1965. Use of spin echoes in a pulsed magnetic-field gradient to study anisotropic, restricted diffusion and flow. J. Chem. Phys. 43 (10), 3597–3603.

Stejskal, E.O., Tanner, J.E., 1965. Spin diffusion measurements: spin echoes in the presence of a time-dependent field gradient. J. Chem. Phys. 42 (1), 288–292.

Tournier, J.D., Calamante, F., Gadian, D.G., Connelly, A., 2004. Direct estimation of the fiber orientation density function from diffusion-weighted MRI data using spherical deconvolution. NeuroImage 23, 1176–1185.

Tuch, D.S., 2004. q-ball imaging. Magn. Reson. Med. 52, 1358–1372.

Tuch, D.S., Weisskoff, R.M., Belliveau, J.W., Wedeen, V.J., 1999. High angular resolution diffusion imaging of the human brain. Proc. of the 7th Annual Meeting of ISMRM, Philadelphia, p. 321.

Tuch, D.S., Reese, T.G., Wiegell, M.R., Makris, N., Belliveau, J.W., Wedeen, V.J., 2002. High angular resolution diffusion imaging reveals intravoxel white matter fiber heterogeneity. Magn. Reson. Med. 48 (4), 577–582.

Tuch, D.S., Reese, T.G., Wiegell, M.R., Wedeen, V.J., 2003. Diffusion MRI of complex neural architecture. Neuron 40, 885–895.

von dem Hagen, E.A.H., Henkelman, R.M., 2002. Orientational diffusion reflects fiber structure within a voxel. Magn. Reson. Med. 48 (3), 454–459.

Wedeen, V.J., Reese, T.G., Tuch, D.S., Weigel, M.R., Dou, J.G., Weiskoff, R.M., Chessler, D., 2000. Mapping fiber orientation spectra in cerebral white matter with Fourier transform diffusion MRI. Proc. of the 8th Annual Meeting of ISMRM, Denver, p. 82.